ACS OMEGA

Article

http://pubs.acs.org/journal/acsodf

Nickel Complexes of C-Substituted Cyclams and Their Activity for CO_2 and H^+ Reduction

Timothy D. Cook,[†] Sarah F. Tyler,[†] Caitlyn M. McGuire,[‡] Matthias Zeller,[†] Phillip E. Fanwick,[†] Dennis H. Evans,[†] Dennis G. Peters,[‡] and Tong Ren*[,†]

[†]Department of Chemistry, Purdue University, 560 Oval Drive, West Lafayette, Indiana 47907, United States

[‡]Department of Chemistry, Indiana University Bloomington, 800 E Kirkwood Avenue, Bloomington, Indiana 47405, United States

Supporting Information

ABSTRACT: Several nickel(II) complexes of cyclams bearing aryl groups on the carbon backbone were prepared and evaluated for their propensity to catalyze the electrochemical reduction of CO_2 to CO and/or H^+ to H_2, representing the first catalytic analysis to be performed on an aryl−cyclam metal complex. Cyclic voltammetry (CV) revealed the attenuation of catalytic activity when the aryl group bears the strong electron-withdrawing trifluoromethyl substituent, whereas the phenyl, *p*-tolyl, and aryl-free derivatives displayed a range of catalytic activities. The gaseous-product distribution for the active complexes was determined by means of controlled-potential electrolysis (CPE) and revealed that the phenyl derivative is the most active as well as the most selective for CO_2 reduction over proton reduction. Stark differences in the activity of the complexes studied are rationalized through comparison of their X-ray structures, absorption spectra, and CPE profiles. Further CV studies on the phenyl derivative were undertaken to provide a kinetic insight.

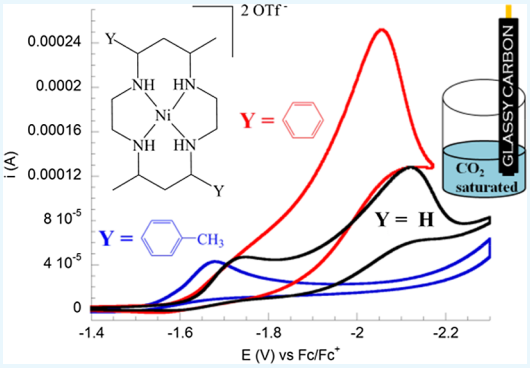

INTRODUCTION

Electrochemical reduction of CO_2 to give reduced carbon fuel sources has been extensively studied over the last several decades as a possible route to a renewable carbon fuel cycle.[1−6] Although the ideal solution would be to employ a light-driven system analogous to photosynthesis, electrocatalysis is a simpler surrogate for convenient evaluation of catalyst candidates, and it can easily be incorporated in a renewable energy scheme, given that the injected electrons are derived from renewable sources such as photovoltaics, wind turbines, and so forth.[4] Many transition-metal complexes have been shown to reduce CO_2, producing predominantly CO and formate as the reduced carbon products. The majority of these systems feature heavy-metal active sites such as Re,[7−9] Ru,[10−14] Ir,[15,16] or Pd,[17,18] and many exhibit low tolerance under aqueous conditions, preferentially producing H_2 in these cases. Nonetheless, many notable examples of CO_2 reduction/activation by 3d metal complexes have appeared in recent years. Savéant and co-workers have demonstrated that the introduction of phenol substituents in Fe-tetraphenylporphyrin improves the efficiency of reduction of CO_2 to CO dramatically.[19−21] More recently, copper porphyrin immobilized on a carbon paper was found capable of reducing CO_2 to hydrocarbons.[22] Berben and co-workers have studied the selective reduction of CO_2 to formate using $[Fe_4N(CO)_{12}]^-$ in great detail.[23−25] Guan and co-workers have investigated the reduction of CO_2 to methanol by borane with Ni and Fe pincer complexes as catalysts.[26,27] Kemp and co-workers investigated CO_2 capture using both main group metal complexes[28,29] and frustrated Lewis pairs[30] and more recently the reduction of CO_2 to CO using a Zn(II) electrocatalyst.[31] Li and co-workers reported photoreduction of CO_2 to CO catalyzed by Co^{III}(cyclam) immobilized on titania.[32] Remarkable efficiency of CO_2 reduction catalyzed by cobalt porphyrins embedded in covalent organic frameworks was recently disclosed by Lin and co-workers.[33]

Of the earth-abundant transition-metal catalysts, Ni(cyclam) (cyclam = 1,4,8,11-tetraazacyclotetradecane) is the most active for the production of CO from CO_2 and compares favorably even with its fourth and fifth row organometallic competitors.[5] Furthermore, Ni(cyclam) and many of its derivatives display selective production of CO over H_2 even under purely aqueous conditions. For nearly two decades, the CO_2 reduction capabilities of Ni(cyclam) and its analogues were almost exclusively studied with a Hg working electrode, with a surface-bound Ni^I species assigned as the putative active catalytic species.[34,35] Use of a toxic Hg working electrode has been pervasive despite early observations by Fujihira and co-workers that a catalytic wave can indeed be observed at a more environmentally benign glassy carbon electrode.[34,36,37] Although the earlier work by Fujihira did not establish the identity of the reduction products for a glassy carbon working electrode, Froehlich and Kubiak recently verified that CO is the major electrolysis product via controlled-potential electrolysis (CPE) coupled with the gas chromatographic analysis of

Received: June 30, 2017
Accepted: July 17, 2017
Published: July 26, 2017

DOI: 10.1021/acsomega.7b00714
ACS Omega 2017, 2, 3966−3976

Scheme 1. Synthesis of Complexes 1−4

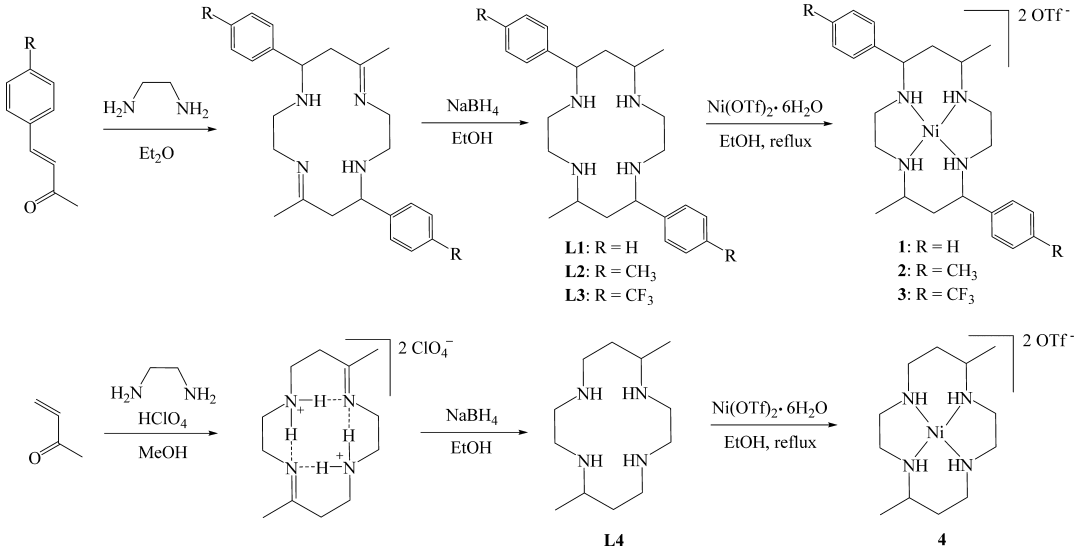

headspace gases.[38] A litany of derivatives was prepared and evaluated by Fujita and co-workers with a Hg electrode, and these derivatives largely consisted of different degrees of methylation along the carbon backbone of the macrocycle.[35] Nonetheless, no method was developed that allowed for simple, systematic functionalization of the macrocycle backbone.[35,37]

Derivatization of the catalyst through substitution on the macrocycle is advantageous in tuning electronic as well as steric parameters for the binding and reduction of CO_2. Prior to this work, functionalization of the cyclam ligand was achieved through N or C substitution of the ring backbone.[35,37,39,40] It was shown that the CO_2 reduction activity diminishes with an increasing degree of N-alkylation.[41] On the other hand, certain C substitutions of the tetraazacyclotetradecane ring have resulted in enhanced activities.[35] In this work, we present several derivatives with pendant aryl groups on the macrocycle, allowing for facile tuning of the sterics and electronics of the catalyst by a change of the substituent on the aryl groups. To our knowledge, no aryl-substituted derivatives of Ni(cyclam) have ever been analyzed for their propensity to reduce CO_2 and/or H^+ electrocatalytically, and the complexes studied with a glassy carbon electrode have been limited to the work of Froehlich and Kubiak with Ni(cyclam) and its N-di- and tetramethyl derivatives.[38]

RESULTS AND DISCUSSION

Synthesis. The synthesis of complexes **1**−**3** (shown in Scheme 1) began with a modular approach adapted from the literature procedures to construct aryl-substituted cyclams with functional group flexibility.[42−44] The desired aryl moieties can be installed simply through the use of the appropriate substituted benzylideneacetone, of which a large variety is accessible through the aldol condensation of the corresponding benzaldehyde derivative with acetone. Cyclization is then achieved by the reaction of benzylideneacetone with ethylenediamine to give the diimine macrocycle. In some cases, the monohydroperchlorate salt of ethylenediamine is used to prevent undesired side reactions, forming the macrocycle as the dihydroperchlorate salt. Reduction of the imine bonds by $NaBH_4$ gives dimethyl, diaryl cyclam derivatives in a reasonable yield. These ligands readily bind $Ni(OTf)_2$ after a simple reflux in EtOH to yield the corresponding Ni complexes. Although **1** has been previously reported as NO_3^- and ClO_4^- salts,[45] **2** and **3** represent novel Ni(cyclam) derivatives, though **L2** is also a known complex.[43] Nevertheless, despite the wide variety of substituted $Ni(cyclam)^{2+}$ species analyzed by Fujita and co-workers, no aryl-substituted $Ni(cyclam)^{2+}$ has ever been evaluated for its ability to catalyze the reduction of CO_2. To further understand the effect of aryl groups on the catalytic activity, aryl-free dimethylcyclam complex **4** was synthesized through adaptation of literature procedures.[46] The ClO_4^- salt of complex **4** has been shown to reduce CO_2 at a Hg electrode,[47] but its activity at a glassy carbon working electrode has not been established, and thus, **4** serves as a useful point of comparison in running parallel analyses with **1**−**3**.

Molecular Structures. X-ray quality single crystals were grown via slow diffusion of Et_2O into a solution of **1** in MeCN and slow diffusion of hexanes into a solution of **2** in EtOAc. Their molecular structures (shown in Figures 1 and 2) revealed significant structural heterogeneity, despite a high degree of constitutional homology. Surprisingly, the addition of a methyl group on the periphery of the macrocycle appears to have a profound effect on the ligand conformation of the coordinated Ni complex. Although **1** displays canonical trans-III, RRSS

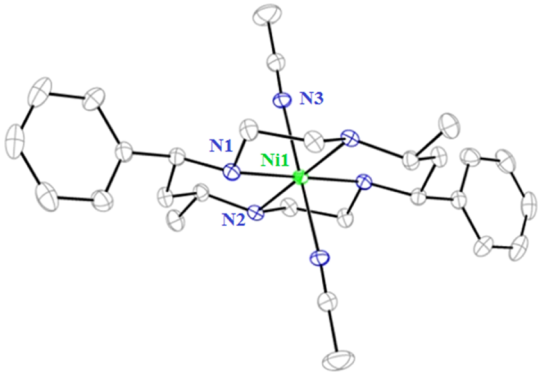

Figure 1. Molecular structure of **1** at 30% probability level. Hydrogen atoms and the two triflate counterions have been removed for clarity. Selected bond lengths (Å): Ni1−N1, 2.093(2); Ni1−N2, 2.080(2); and Ni1−N3, 2.107(2).

DOI: 10.1021/acsomega.7b00714
ACS Omega 2017, 2, 3966−3976

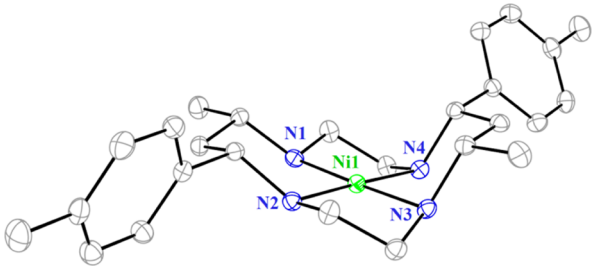

Figure 2. Molecular structure of **2** at 30% probability level. Hydrogen atoms and the two triflate counterions have been removed for clarity. Selected bond lengths (Å): Ni1−N1, 1.9348(19); Ni1−N2, 1.9312(17); Ni1−N3, 1.9171(19); and Ni1−N4, 1.9133(18).

geometry that is ubiquitous among $Ni(cyclam)^{2+}$ derivatives, **2** displays boatlike trans-I, RSRS conformation.[37] Furthermore, **1** demonstrates substantial affinity for axial ligands and seems to prefer an octahedral coordination geometry, as crystals of **1** grown from an EtOH/hexane mixture were found to have axially coordinated triflates (see Figure S7 in Supporting Information) despite the low donicity of the triflate ion. By contrast, **2** does not adopt H_2O or triflates as axial ligands when grown from EtOAc, and attempts to grow a crystal from a MeCN solution were unsuccessful, only resulting in the formation of a yellow oil. Notably, the solution color of **2** is yellow even in coordinating solvents such as MeCN or MeCN/H_2O mixtures. As established previously, octahedral Ni_{cyclam} bis-halo and bis-solvento complexes are blue-violet, whereas the square-planar complexes are yellow-orange.[48−51] The combined effects of ring conformation and increased electron density due to the tolyl group give the Ni center in **2** an apparent preference for a square-planar rather than an octahedral coordination geometry, whereas **1** clearly prefers octahedral coordination. The effects of the increased electron density provided by the tolyl group are also evident in the Ni−N(cyclam) bond distances of **1** and **2**. The coordinated MeCN molecules for complex **1** have relatively short Ni−N bond lengths [2.107(2) Å], indicating that the axial interactions are nearly as strong as the coordinated amines of the macrocycle itself [2.093(2) and 2.080(2) Å]. Complex **2** has significantly shorter Ni−N bond lengths (1.92 Å on average) as the macrocyclic amines bond more strongly to stabilize the Ni^{II} center in a square-planar setting where it is not supported by any axial ligand.

A crystal of **3** suitable for X-ray analysis was obtained through slow evaporation of a concentrated solution of the complex in 20% aqueous MeCN, and its molecular structure (Figure 3) was strikingly different from the structures of **1** and **2**. Complex **3** adopts an unusual cis-V, RRRR macrocycle conformation, which is typically only observed with a bidentate supporting ligand.[52] In this case, one H_2O and one MeCN act as the fifth and sixth ligands to give the Ni center an octahedral coordination environment. The Ni−N_{cyclam} bond lengths of **3** are slightly longer than those of **1**, reflecting weaker donation when the ligand is functionalized with the electron-deficient $-CF_3$ groups. The Ni−N_{MeCN} and Ni−O bond lengths [2.125(2) and 2.131(2) Å, respectively] are also slightly longer than the Ni−N_{MeCN} bonds observed for **1** [2.107(2) Å]. Complex **3** again highlights the sensitivity of the macrocycle conformation toward substitution. The structure of **4** has been reported previously as the Cl^- salt and displays the conventional trans-III macrocycle conformation.[53] As the triflate salt, **4**

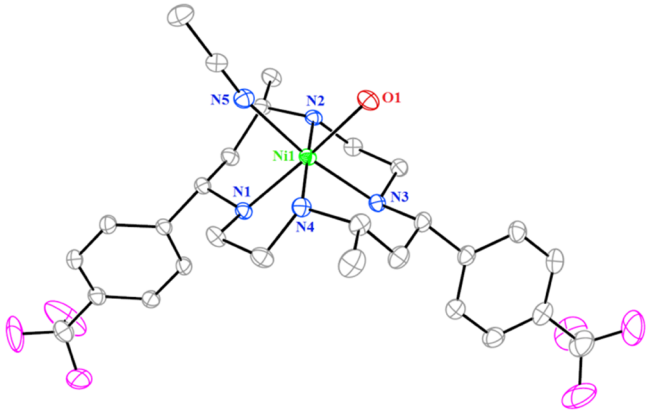

Figure 3. Molecular structure of **3** at 30% probability level. Hydrogen atoms and the two triflate counterions have been removed for clarity. Selected bond lengths (Å): Ni1−N1, 2.132(2); Ni1−N2, 2.086(2); Ni1−N3, 2.120(2); Ni1−N4, 2.088(2); Ni1−N5, 2.125(2); and Ni1−O1, 2.1306(19).

was isolated as an orange solid and gives an orange solution in MeCN, indicating the lack of axial triflate or solvent coordination.

Ultraviolet−Visible (UV−Vis) Absorption Spectra. Given the established relationship between the solution color and coordination geometry of Ni(tetramine) complexes discussed above, visible-light absorption spectroscopy is an effective method for probing the solution geometry of these complexes. In solution, Ni(cyclam) complexes exist in a spin-state equilibrium between the diamagnetic, square-planar conformation and the octahedral, paramagnetic conformation, where the population of each state is affected by several factors such as solvent, counterion, and electrolyte concentration.[51] UV−vis absorption spectra were collected for **1**−**4** in a 20% aqueous MeCN solution and are shown in Figure 4.

As expected, there is a clear difference between the UV−vis spectra of the complexes that are purple as solids (**1** and **3**) and those that are yellow-orange (**2** and **4**). Complexes **2** and **4** exhibit prominent peaks at 453 and 456 nm, respectively,

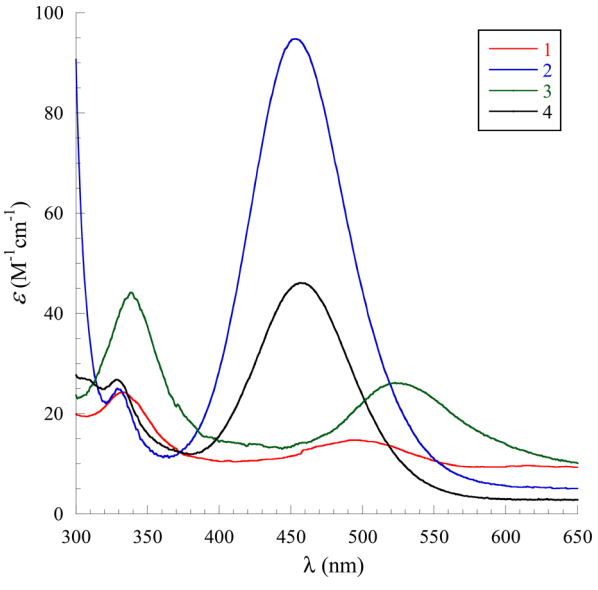

Figure 4. UV−vis absorption spectra of **1**−**4** in 20% aqueous MeCN.

DOI: 10.1021/acsomega.7b00714
ACS Omega 2017, 2, 3966−3976

corresponding to the d−d band of the square-planar conformation in the diamagnetic spin state. This peak is completely absent from the spectra of **1** and **3**. By contrast, the spectra for complexes **1** and **3** exhibit d−d bands at 497 and 523 nm, indicative of an octahedral geometry and a high-spin, paramagnetic state. All four complexes have a second absorption peak between 329 and 339 nm, which corresponds to the d−d transition of the octahedral, high-spin species, although for **1** and **3**, this band is more intense relative to the d−d bands at longer wavelengths. Thus, it can be concluded that, whereas all of the complexes have at least minor contributions from the high-spin state, only **2** and **4** show an appreciable population of the diamagnetic state.

Solution Voltammetry. As shown in Figure 5, the cyclic voltammograms of **1**−**4** all display distinct behavior despite

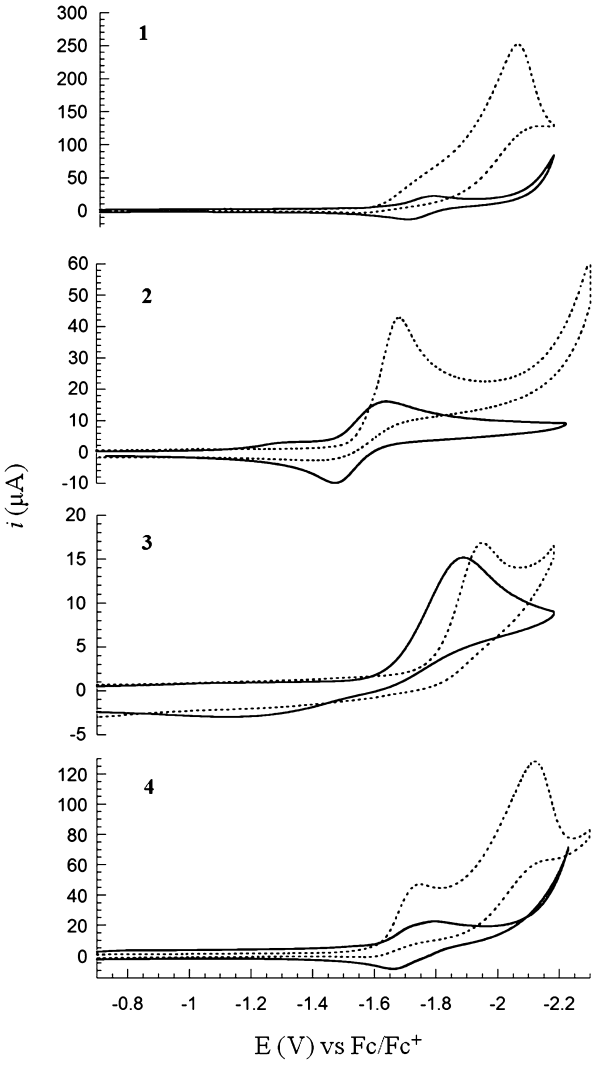

Figure 5. Cyclic voltammograms of 1.0 mM solutions of **1**−**4** in a 0.08 M solution of Bu_4NPF_6 in 20% aqueous MeCN, purged with Ar (solid trace) or CO_2 (dotted trace).

their structural homology. Subtle differences in the macrocycle substitution lead to significant, somewhat counterintuitive differences in the Ni-based reduction potentials under Ar. Each complex displays a single one-electron cathodic peak as well as a single one-electron anodic peak (see Figure S8 in Supporting Information for the background scans under Ar and CO_2). These waves are assigned as the $Ni^{II/I}$ and $Ni^{II/III}$ couples. Whereas the $Ni^{II/III}$ process is reversible for all complexes, the $Ni^{II/I}$ transition is reversible for **1**, **2**, and **4** but not **3**. Curiously, the trend in reduction potentials does not seem to match the intuition that, in a set of analogous complexes, the species bearing the most electron-withdrawing substituent will have the least negative reduction potential under Ar as it is more readily reduced at the cathode. Accordingly, **3** should have the least negative reduction potential by virtue of the electronegative trifluoromethyl groups. Complex **1** would be the next most electron-deficient because of the phenyl groups, and complexes **2** and **4** would be the least electron-deficient of the series and are expected to have similar reduction potentials because the donicity of a methyl substituent on the aryl group will somewhat counteract the inductive electron-withdrawing effect of the aryl group, causing little net change in the expected reduction potential. Instead, the opposite trend is observed; **3** has the most negative reduction potential followed by **1**, then **4**, and finally, **2** has the least negative $Ni^{II/I}$ potential of the series. Clearly, the expected electron deficiency of the macrocycle is not the only factor governing these $Ni^{II/I}$ reduction potentials, and a delicate interplay between the geometry and strength of the axial ligands, which could potentially be triflate, MeCN, or H_2O under these conditions, likely explains this deviation. The differential donation strength of these ligands is expected to affect the $Ni^{II/I}$ potentials of the complexes and likewise their reactivity toward CO_2 because of the variation in the reducing strength of the Ni^{I} complex. By contrast, the $Ni^{II/III}$ potentials do follow the intuitive trend: the oxidation potentials shift anodically as the macrocycle becomes more electron-deficient, with the most positive $Ni^{II/III}$ potential observed for **3**, followed by **1**, **2**, and finally **4**.

Although the cyclic voltammograms under Ar for these otherwise similar complexes are surprisingly disparate, the effect of macrocycle substitution is even more pronounced when the voltammograms are recorded under a CO_2 atmosphere. As shown in Figure 5 (dotted traces), complexes **1**, **2**, and **4** all display a similar behavior for the $Ni^{II/I}$ couple under CO_2; the reversible redox couple under Ar is completely irreversible under CO_2, with a substantial increase in the cathodic peak current. This increase in current, referred to as the "catalytic current" under CO_2, is indicative of an electrocatalytic reaction, as significantly more current is passed than would be expected for a simple one-electron reduction of the Ni^{II} center. By contrast, the current for the $Ni^{II/I}$ couple does not increase appreciably for complex **3**, implying that no catalytic process takes place under CO_2. The lack of activity of **3** is likely due to the irreversible nature of its reduction under Ar; the product of the reduction of **3** simply may not be stable enough to bind and reduce CO_2 appreciably. Complex **2** has a distinctive profile under CO_2, in which the catalytic current is approximately 3 times the current under Ar, and only one sharp peak is visible. Complexes **1** and **4** have a similar threefold increase in current at the $Ni^{II/I}$ potential; however, at more negative potentials, a second, distinct cathodic peak is observed in the cyclic voltammograms. This second peak suggests that a different catalytic process is accessible at more negative potentials under CO_2, which could be assigned as reduction of H^+ to H_2 because of acidification of the aqueous media caused by saturation with CO_2 or could possibly be a different catalytic pathway for the reduction of CO_2. Others have reported this "second peak" in similar systems, but its origin is still not completely under-

DOI: 10.1021/acsomega.7b00714
ACS Omega 2017, 2, 3966−3976

stood.[36,38] Additionally, the cyclic voltammogram of complex **1** under CO_2 in neat acetonitrile (Figure S9 in Supporting Information) does reveal an irreversible $Ni^{II/I}$ couple with current comparable to that recorded under Ar, indicating the absence of catalytic activity without water or other proton source.

As shown in Figure 6, catalytic currents for the $Ni^{II/I}$ couple are of nearly identical magnitude for the three active

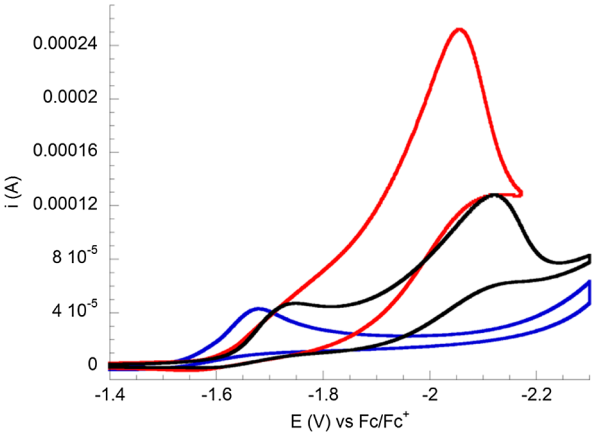

Figure 6. Cyclic voltammograms of **1** (red trace), **2** (blue trace), and **4** (black trace) in a 0.08 M solution of Bu_4NPF_6 in 20% aqueous MeCN, saturated with CO_2.

electrocatalysts **1**, **2**, and **4**. Although no further catalytic current is observed at more negative potentials for **2**, the current increases steadily to a second catalytic peak for **1** at more negative potentials, and the "peak" for the $Ni^{I/II}$ couple is not well-resolved and appears more as a shoulder. For **4**, the current after the first catalytic peak dips slightly before increasing steadily to a second catalytic peak. This difference in profile suggests that for **1**, the shoulder and the "second" catalytic peak may be representative of a single catalytic mechanism or pathway for **1**, whereas the clear resolution of the first and second catalytic peaks for **4** suggests that these two peaks represent distinct mechanisms and/or product pathways in operation for **4** at these different peak potentials. As can be seen in Figure 6, complex **1** clearly is the most active of the three electrocatalysts, with the catalytic peak current almost twice that for complex **4**. In fact, complex **1** reaches the peak current of complex **4** (~120 μA) at a potential over 200 mV less negative than the potential for the second catalytic peak of **4**, and **1** maintains a higher current between the first and second catalytic waves than **4**. These observations clearly indicate that **1** is the most active catalyst of the series under these conditions, making **1** the natural candidate for further cyclic voltammetry (CV) studies discussed in detail later.

CPE. Although the cyclic voltammograms shown in Figures 5 and 6 clearly establish the electrocatalytic activities of **1**, **2**, and **4** under CO_2, the composition of the reduction products cannot be established through this method. To truly evaluate the activity of these complexes for the conversion of CO_2 to reduced carbon products, CPE coupled with headspace gas analysis was performed by use of a gas-tight electrochemical cell described elsewhere.[54] Although glassy carbon electrodes are convenient for use in small electrochemical cells, CPE cells often necessitate large, porous electrodes to achieve a complete and efficient electrolysis of the analyte. In this study, a reticulated vitreous carbon (RVC) disc was selected as the working electrode for the CPE experiments. The potential was held at −1.7 V versus Fc^+/Fc for each complex, which is slightly more negative than that of the $Ni^{II/I}$ couple of **2** and slightly less negative than those of the $Ni^{II/I}$ couples of **1** and **4**. After 30 min of electrolysis, the headspace was sampled and injected directly into a gas chromatograph with a thermal conductivity detector (GC−TCD) to identify and quantify the gaseous products present. When electrolyses were performed at more negative potentials, H_2 production directly from the RVC electrode surface dominated the current response prior to the addition of the catalyst; as a result, the current response and product distribution upon catalyst addition could not be adequately resolved from this "background" activity of the working electrode. Unfortunately, this precluded further analysis of the second catalytic wave that appears beyond −2.0 V. Table 1 shows the gaseous product distributions for **1**, **2**, and **4**, as well as their Faradaic and catalytic efficiencies.

In agreement with its cyclic voltammogram under CO_2, **1** is the most CO-producing catalyst. Complex **2** is the least active of the series and displays poor selectivity for the reduction of CO_2 over H^+. The total charge passed by **2** is comparable to the total charge passed by a solution without a catalyst present, which suggests that much of the current and H_2 observed during the electrolysis of **2** may be due to direct reduction on the RVC electrode surface. Complex **4** actually appears to be selective for the reduction of H^+ and produces much less CO in comparison. The amount of charge passed during the electrolysis of **4** is much higher than the charge passed during the electrolysis of the blank solution; hence, it is reasonable to conclude that **4** is truly selective for H_2 production rather than CO. In addition to the high catalytic activity, complex **1** is also the most selective for CO production, with 80% FE for CO and only 7% for H_2. Complex **1** is the only complex which completes multiple turnovers of CO_2 to CO during the electrolysis period, establishing true catalysis. In comparison, **2** and **4** reduce CO_2 quite sluggishly and produce less than 1

Table 1. CPE Data for 1, 2, and 4[a]

complex	Q (C)	FE, CO (%)	FE, H_2 (%)	TON, CO	TON, H_2
1	21.2 ± 0.7	80.0 ± 3.5	7.3 ± 0.5	4.5 ± 0.3	0.4 ± 0.0
2	2.7 ± 0.3	29.1 ± 8.4	44.1 ± 2.8	0.25 ± 0.11	0.37 ± 0.09
4	23.7 ± 2.1	10.3 ± 0.4	53.4 ± 1.1	0.64 ± 0.1	3.3 ± 0.4
blank	2.9	1	77		

[a]Performed in CO_2-saturated solutions of 20% aqueous MeCN with 0.08 M NBu_4PF_6; data reported as the average of 2 trials; solutions were electrolyzed for 30 min, and headspace gases were analyzed via GC−TCD. Q = total charge passed, Faradaic efficiency (FE) $= \frac{\text{charge to form product}}{\text{total charge passed}}$, and turnover number (TON) $= \frac{\text{mol product}}{\text{mol catalyst}}$

DOI: 10.1021/acsomega.7b00714
ACS Omega 2017, 2, 3966−3976

equiv of CO per mol catalyst during the electrolysis period. Likewise, only **4** reduces H^+ to H_2 catalytically, with **1** and **2** producing sub-stoichiometric quantities of H_2, most of which is likely to be generated directly on the working electrode surface. The reactivity of **4** highlights the importance of the electrode material for this family of catalysts as the perchlorate salt of **4** was previously found to be highly active for CO production at a Hg electrode, forming a negligible quantity of H_2 in this case.[47] Because the outcome of CPE experiments may vary significantly depending on the setup of the electrolysis cell and the nature of the working electrode, the catalytical activity of Ni(cyclam)Cl_2 was examined under conditions identical to those used for **1**, **2**, and **4**, yielding FEs of 35 and 66% for CO and H_2, respectively (the detailed results are provided in Table S1 in the Supporting Information). Clearly, **1** is a far better catalyst than Ni(cyclam)Cl_2 in terms of both the selectivity and turn-over number for CO production under the same conditions. It should be noted that the quantity of H_2 produced during the electrolysis of **1** is commensurate with the H_2 production by the blank solution and likely stems directly from the working electrode.

This dramatic difference in the catalytic profile is somewhat unexpected for these otherwise similar systems, though some insight can be gained from the analysis of their CPE behaviors. Notably, **1** is the only catalyst that is purple in the pre-electrolysis solution, whereas **2** and **4** are yellow. After the completion of electrolysis, the solution color is unchanged for **1**, whereas **2** and **4** gradually develop a green color over time. Opening the cell to an ambient atmosphere, or applying a potential of 0 V to the cell, causes this green color to dissipate rapidly, suggesting that this green species is a reduced Ni complex, probably Ni^I. Furthermore, there is a concomitant decrease in the current for **2** and **4** as the green color develops, whereas the current stays nearly constant for **1** after a short induction period. These observations suggest that **2** and **4** lose the catalytic activity during the reaction and cannot be cycled properly as they are "trapped" in a Ni^I state that is somehow deactivated. Complex **1** does not seem to suffer the same fate, as the solution color remains unchanged throughout electrolysis, and multiple catalytic turnovers are achieved. Froehlich and Kubiak have demonstrated that Ni(cyclam) becomes inhibited as [CO] increases during electrolysis, forming the inactive $[Ni(cyclam)(CO)]^+$ adduct that cannot continue catalytic cycling.[55] Given that $[Ni(cyclam)]^{2+}$ displays this same "yellow-to-green" solution behavior during electrolysis, it is reasonable to conclude that CO binding is a major degradation pathway for **2** and **4** but does not appreciably affect **1**. We are continuing to explore the fundamental reasons for this apparent improvement in the catalytic efficiency of **1** relative to $Ni(cyclam)^{2+}$, **2**, and **4**, but at present, we suggest that the electron deficiency of **1** relative to **2** and **4** is the predominant cause. CO is usually found as a ligand for low-valent metals, often forming $M^0(CO)$ complexes preferentially. Thus, we postulate that CO might prefer the more electron-rich derivatives **2** and **4**, and **1** could be at an ideal level of electron deficiency such that the Ni^I species is sufficiently electron-rich to bind and reduce CO_2 but not electron-rich enough to bind CO strongly and thus inhibit catalysis. A second rationale, which does not invoke CO binding, can be proffered on the basis of the UV–vis spectra of the complexes. Although **1** is present in solution as the high-spin octahedral species under these conditions, the vast majority of **2** and **4** are present as the square-planar, diamagnetic species, with only minor contributions from the octahedral state. Hence, it is reasonable to conclude that upon reduction to Ni^I, orbital rearrangement must occur from the square-planar state to allow for binding of CO_2 as a fifth ligand for **2** and **4**, whereas **1** circumvents this energy barrier and allows for ligand exchange between CO_2 and the octahedral species. Indeed, the square-planar conformation may be totally inactive in these complexes, and the observed activities of **2** and **4** may originate only from the minor population of the octahedral high-spin state that is observed in solution under these conditions.

Kinetics Study Based on CV. The CPE results are both less informative on reaction rates and hard to be compared with other published results because of the differences between the electrolytic cells and conditions. On the other hand, CV has been shown to be a powerful tool to yield accurate kinetic data and mechanistic insights for electrocatalysis by many groups, especially those of DuBois on H^+ reduction[56] and Berben[57] and Fujita on CO_2 reduction.[35] Inspired by these successful investigations, a series of CV experiments have been carried out to further investigate the kinetics of the best catalyst, **1**.

First, a series of CVs were recorded with the scan rates (ν) varying from 0.005 to 0.045 V s^{-1} under an Ar atmosphere (Figure 7a). It is clear from Figure 7b that the current density for the $Ni^{II/I}$ couple increases linearly as a function of $\nu^{1/2}$, indicating not only a reversible electron transfer but also a diffusion-controlled, one-electron redox reaction.[58] This linearity also signals the absence of catalytic activity during the time scale of the CV experiment under Ar. Hence, H_2 evolution only occurs on longer time scale experiments such as CPE, which even then only produces H_2 with a FE of 7%.[23,57] The linear relationship can be further analyzed according to the Randles–Sevcik equation (eq 1), where, at 25 °C, J_p is the current density (A cm^{-2}), n is the number of electrons transferred (n = 1), D is the diffusion coefficient for **1** (cm^2 s^{-1}), and C is the bulk concentration of **1** (mol cm^{-3}). Using the slope of J_p versus $\nu^{1/2}$, the diffusion coefficient for **1** was found to be 4.7×10^{-5} cm^2 s^{-1}.[58]

$$J_p = (2.686 \times 10^5) n^{3/2} D^{1/2} C \nu^{1/2} \quad (1)$$

The current density dependence on the scan rate was also studied under a CO_2 atmosphere (Figure 8), which allows for the use of eq 2 to determine the rate constant, k_{cat} (mol^{-1} cm^3 s^{-1}), for the entire catalytic reaction, assuming that the overall catalytic reaction is second-order.[57]

$$\frac{J_{cat}}{J_p} = \left(\frac{n}{0.446}\right)\sqrt{\left(\frac{RTk_{cat}[CO_2]}{F\nu}\right)} \quad (2)$$

J_{cat} and J_p are the current density of the Ni-based reduction under CO_2 and Ar (A cm^{-2}), respectively, n is the number of electrons required for the catalytic reaction (n = 2), R is the gas constant (8.314 J K^{-1} mol^{-1}), T is the temperature (298 K), F is Faraday's constant (96485.3 C mol^{-1}), ν is the scan rate (V s^{-1}), and the concentration of CO_2 is 0.00019 mol cm^{-3}.[55]

A linear dependence of J_{cat}/J_p on $\nu^{-1/2}$ is clear from Figure 8a, and the slope therein can be used to determine k_{cat}. The calculated k_{cat}, a second-order rate constant, was found to be 2.754 M^{-1} s^{-1} (2.754×10^3 mol^{-1} cm^3 s^{-1}). The turn-over frequency (TOF) was estimated to be 0.523 s^{-1} (1884 h^{-1}, $[CO_2]$ = 0.19 M) based on k_{cat} using eq 3.

$$TOF = k_{cat}[CO_2] \quad (3)$$

DOI: 10.1021/acsomega.7b00714
ACS Omega 2017, 2, 3966–3976

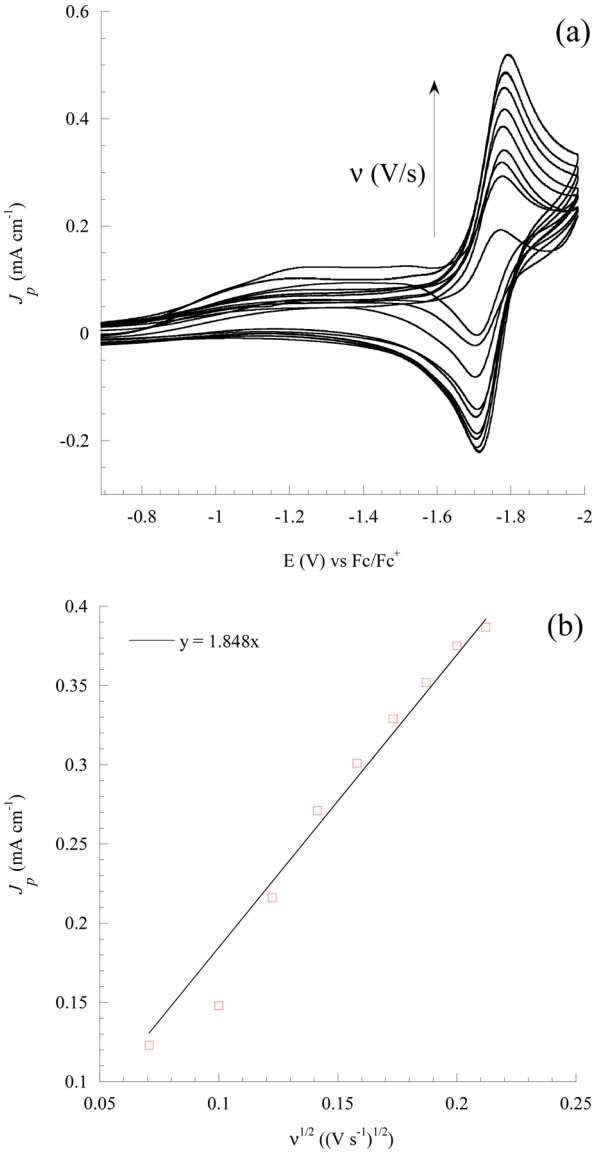

Figure 7. (a, Top) CVs of **1** in 0.08 M Bu_4NPF_6 of 20% aqueous MeCN under Ar at varying scan rates (0.005−0.045 V s^{-1}) and (b, bottom) plot of J_p vs $\nu^{1/2}$ for **1**.

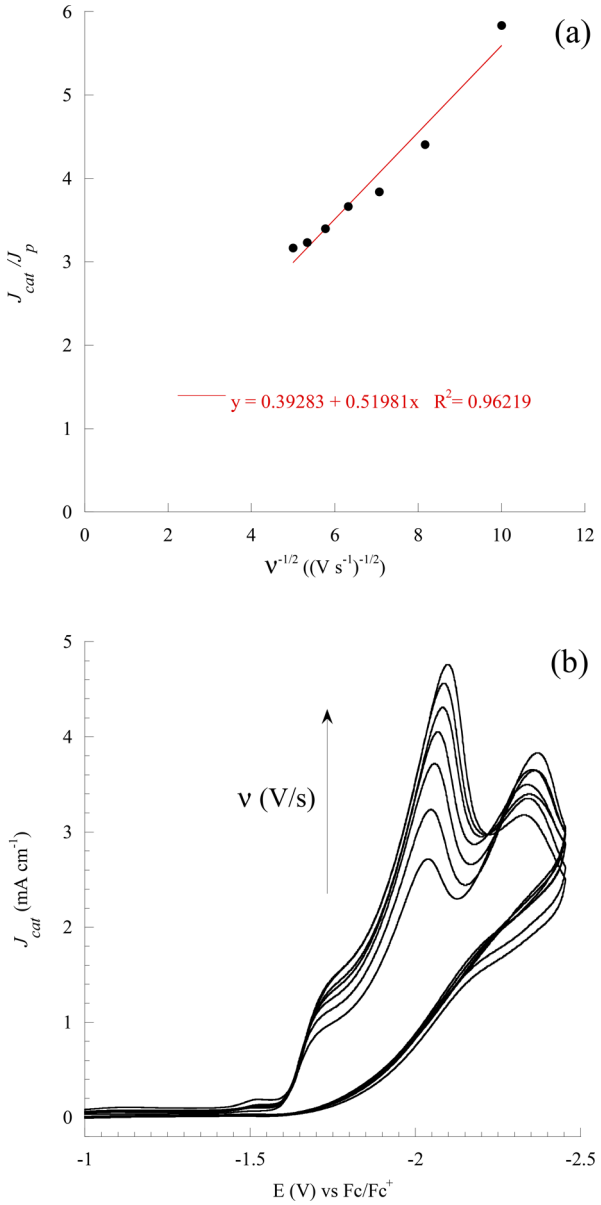

Figure 8. (a, Top) Plot of J_{cat}/J_p vs $\nu^{-1/2}$ for **1** under CO_2 and (b, bottom) CVs of **1** in 0.08 M Bu_4NPF_6 of 20% aqueous MeCN under CO_2 with scan rates ranging from 0.010 to 0.04 V s^{-1}.

The bimolecular nature of the overall reaction is validated by CV studies wherein the catalyst concentration (Figure 9) and the CO_2 concentration (Figure 10) were varied separately. As shown in Figure 9a, the catalytic current density increases linearly with increasing [**1**]. Similarly, a linear relationship exists between the catalytic current density and $[CO_2]^{1/2}$ ($M^{-1/2}$, Figure 10a). These linear relationships are indicative that the catalytic reaction is first-order with respect to the concentration of **1** and half-order with respect to the CO_2 concentration.[57]

$$J_{cat} = 2F[cat]\sqrt{D_{cat}k_{cat}[CO_2]} \quad (4)$$

CONCLUSIONS

In summary, a series of C-aryl-substituted Ni(cyclam) derivatives have been synthesized through adaptation of literature procedures, providing a facile route to derivatization of the macrocyclic ligand. These complexes are the first aryl derivatives of Ni(cyclam) to be evaluated for their ability to reduce CO_2 catalytically. Similar to Ni(cyclam), complexes **1**, **2**, and **4** do not require a Hg electrode for activity and allow the use of environmentally benign carbon working electrodes. Electrochemistry of these complexes demonstrated that the electron-withdrawing substituents on the aryl group deactivate the Ni center toward reduction of CO_2 and H^+, whereas the other derivatives display surprisingly disparate levels of catalytic activity, with the phenyl derivative **1** demonstrating the highest activity for CO_2 reduction. The dramatic increase in the CO_2 reduction activity for **1** over **2** and **4** may be tentatively attributed to the differential CO binding at the Ni^I state and/or differential population of the high-spin octahedral and diamagnetic square-planar states in solution, and our efforts are ongoing to verify and elucidate the nature of these interactions. Further CV studies of **1** under various reaction conditions reveal that the electrocatalytic reaction is first-order with respect to the catalyst concentration and half-order with respect to the CO_2 concentration.

DOI: 10.1021/acsomega.7b00714
ACS Omega 2017, 2, 3966−3976

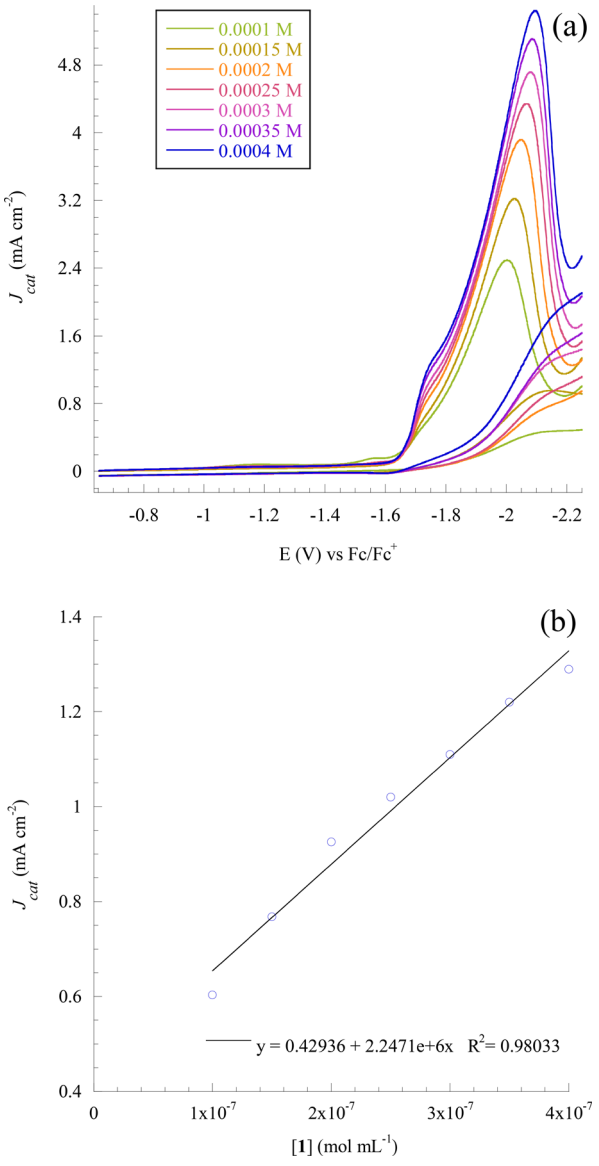

Figure 9. (a, Top) CVs under a CO_2 atmosphere with [**1**] varying from 0.0001 to 0.0004 M in 0.08 M Bu_4NPF_6 of 20% aqueous MeCN with a scan rate of 0.1 V s^{-1} and (b, bottom) plot of current density (J_{cat}) vs [**1**] (mol mL^{-1}).

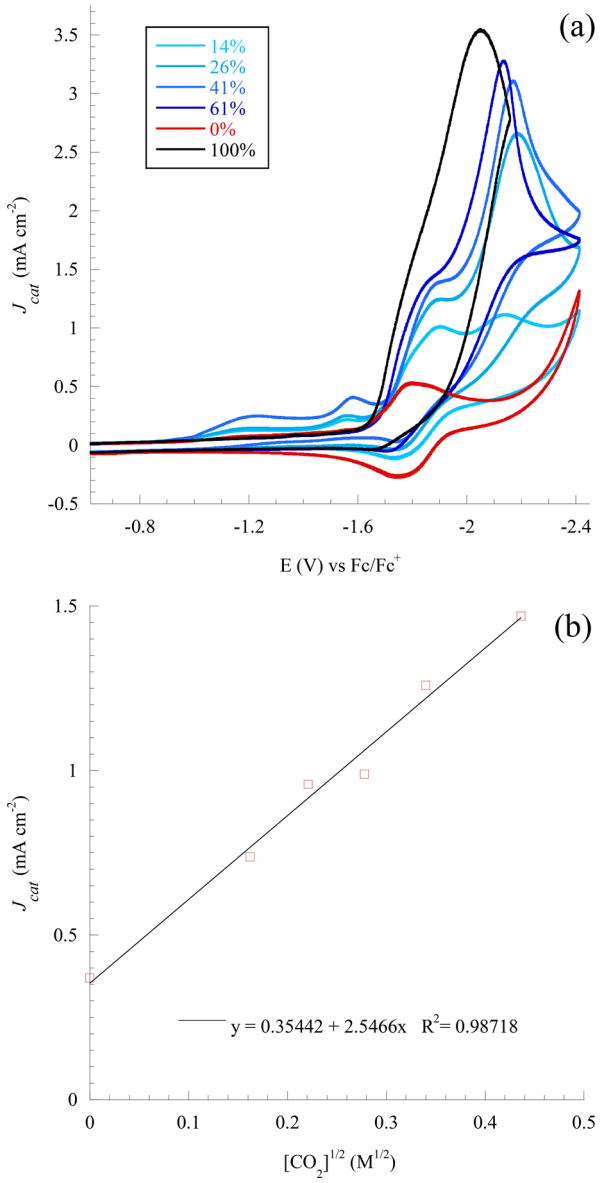

Figure 10. (a, Top) CVs of **1** in 0.1 M Bu_4NPF_6 of 20% aqueous MeCN with varying concentrations of CO_2 (0, 14, 26, 41, 61, and 100%) with a scan rate of 0.1 V s^{-1}. The concentration of CO_2 delivered to the CV cell was controlled by the outlet pressure of the gas regulator and balanced with Ar gas, maintaining a pressure of approximately 1 atm. The CO_2 and Ar gases were mixed in a round-bottom flask for 15 min before the mixture was purged through the CV solution for 15 min. (b, bottom) Plot of J_{cat} vs [CO_2]$^{1/2}$ (M$^{1/2}$). Note: the data point for 0% [CO_2] is not J_{cat} but rather J_p under Ar.

EXPERIMENTAL SECTION

General Procedures. Ketone precursors for **L1**−**L3** were synthesized according to the literature procedure and further purified by vacuum distillation at 90 °C and 100 mTorr.[59] **L1**,[43] 4,14-dimethyl-7,12-diphenyl-1,4,8,11-tetraazacyclotetradeca-4,14-diene,[42] **L2**,[43] and 4,14-dimethyl-1,4,8,11-tetraazacyclotetradeca-4,14-diene dihydroperchlorate[46] were prepared according to literature procedures. All reagents were used as received. Proton nuclear magnetic resonance (^{1}H NMR) spectra were obtained with a Varian Mercury300 NMR instrument, with chemical shifts (δ) referenced to the residual solvent signal ($CHCl_3$ at 7.27 ppm). UV−vis spectra were obtained with a JASCO V-670 spectrophotometer. Gas chromatography data were collected on an Agilent 7890A instrument with a TCD and an HP-Molsieve column (length = 30 m, diameter = 0.320 mm, and film thickness= 12.0 μm). Electrospray mass spectra were obtained as electrospray in a positive-ion mode with the aid of a Waters Micromass ZQ4000 instrument. Cyclic voltammograms were recorded at a scan rate of 100 mV s^{-1} on a CHI620A voltammetric analyzer with a glassy carbon working electrode (diameter = 2 mm and area = 0.0314 cm^2), a Pt wire auxiliary electrode, and a Ag wire reference electrode filled with 0.1 M Bu_4NPF_6 in MeCN. Potentials were referenced to a ferrocene internal standard added to the solution at the end of data collection. CPEs were performed with a CHI620A voltammetric analyzer with a Duocel RVC disc (porosity = 100 ppi, diameter = 200 mm, and thickness = 5 mm) as the working electrode, a graphite rod anode, and an Ag wire reference electrode filled with 0.1 M Bu_4NPF_6 in MeCN. The concentration of the analyte was always 1.0 mM.

DOI: 10.1021/acsomega.7b00714
ACS Omega 2017, 2, 3966−3976

4,14-Dimethyl-7,12-di-*p*-tolyl-1,4,8,11-tetraazacyclotetradeca-4,14-diene. (*E*)-4-Tolyl-3-buten-2-one (3.27 g, 0.0204 mol) was dissolved in 50 mL of Et_2O. Ethylenediamine (1.36 mL, 0.0204 mol) was added, and the solution was stirred for 72 h at room temperature, at which point a copious white precipitate was formed. The precipitate was filtered off and dried in vacuum. Yield: 2.8 g, 68%. ESI-MS (MeOH): 405.3 $[M + H]^+$. ^1H NMR ($CDCl_3$, δ): 7.30−7.14 (m, 8H, ArH), 3.97 (t, 2H, CH), 3.06−2.20 (m, 12H, CH_2), 2.10 (s, 6H, $ArCH_3$), 1.43 (s, 6H, CH_3).

4,14-Dimethyl-7,12-di-*p*-(α,α,α-trifluorotolyl)-1,4,8,11-tetraazacyclotetradeca-4,14-diene. (*E*)-4-α,α,α-Trifluorotolyl-3-buten-2-one (4.0 g, 0.019 mol) was dissolved in 80 mL of Et_2O. Ethylenediamine (1.25 mL, 0.0187 mol) was added, and the solution was stirred for 24 h at room temperature. The solvent was removed under reduced pressure to give a yellow solid, which was suspended in Et_2O, filtered, and rinsed with Et_2O until the filtrate became colorless. The white solid was then dried in vacuum. Yield: 4.1 g, 86%. ESI-MS (MeOH): 513.2 $[M + H]^+$. ^1H NMR ($CDCl_3$, δ): 7.61 (d, 4H, ArH), 7.44 (d, 4H, ArH), 4.02 (t, 2H, CH), 2.72 (d, 4H, CH_2), 2.45 (t, 4H, CH_2), 1.73 (t, 4H, CH_2), 1.18 (s, 6H, CH_3).

4,14-Dimethyl-7,12-di-*p*-(α,α,α-trifluorotolyl)-1,4,8,11-tetraazacyclotetradecane (L3). 4,14-Dimethyl-7,12-di-*p*-(α,α,α-trifluorotolyl)-1,4,8,11-tetraazacyclotetradeca-4,14-diene (4.1 g, 0.0080 mol) was dissolved in 140 mL of EtOH. $NaBH_4$ (1.2 g, 0.032 mol) was added in small portions, and the solution was stirred for 3 h at room temperature. The solvent was removed under reduced pressure, and the residue was extracted into $CHCl_3$ and washed with H_2O and brine before the organic layer was dried over Na_2SO_4. After filtration and removal of the solvent, the clear residue was dried under vacuum and recrystallized from minimal Et_2O at −40 °C to give square white crystals. Yield: 3.0 g, 73%. ESI-MS (EtOH): 517.2 $[M + H^+]^+$. ^1H NMR ($CDCl_3$, δ): 7.57 (d, 4H, ArH), 7.41 (d, 4H, ArH), 3.88 (t, 2H, CH), 2.94 (q, 2H, CH_2), 2.69 (d, 4H, CH_2), 2.42 (t, 4H, CH_2), 1.64 (t, 4H, CH_2), 1.01 (d, 6H, CH_3).

4,14-Dimethyl-tetraazacyclotetradecane (L4). 4,14-Dimethyl-tetraazacyclotetradeca-4,14-diene dihydroperchlorate (1.8 g, 0.0055 mol) was suspended in 80 mL of EtOH. $NaBH_4$ (1.0 g, 0.026 mol) was added in small portions and stirred for 3 h at room temperature, causing the solid to dissolve slowly in the effervescent solution. The solvent was removed under reduced pressure, and the residue was extracted into $CHCl_3$ and washed with H_2O and brine, and the organic layer was dried over Na_2SO_4. After filtration and removal of the solvent, the clear residue was dried under vacuum and recrystallized from minimal Et_2O at −40 °C to give white microcrystals. Yield: 0.550 g, 57.0%. ESI-MS (EtOH): 229.2 $[M + H^+]^+$. ^1H NMR ($CDCl_3$, δ): 2.99−2.33 (m, 14H, CH_2, CH), 1.67 (t, 2H, CH_2), 1.48 (q, 2H, CH_2), 1.03 (d, 6H, CH_3).

Ni(L1)(OTf)$_2$ (1). **L1** (0.254 g, 0.668 mmol) was suspended in 50 mL of EtOH. $Ni(OTf)_2{\cdot}6H_2O$ (0.310 g, 0.666 mmol) was added, and the mixture was refluxed for 48 h as the solution color slowly turned orange. The solvent was then reduced to 1−2 mL, and the flask was cooled to −40 °C to maximize precipitation. The resulting purple solid was filtered off and dried in vacuum. Yield: 0.322 g, 65.5%. ESI-MS (EtOH): 587.1 $[Ni(\mathbf{L1})(OTf)]^+$; 437.3 $[Ni(\mathbf{L1})-H^+]^+$. Anal. found (calcd) for: C, 42.60 (42.35); H, 4.96 (4.92); N, 7.74 (7.60). Cyclic voltammetry (MeCN under Ar): $Ni^{II/I}$, $E_{1/2}$ = −1.77 V, $i_{p,c}/i_{p,a}$ = 0.92; $Ni^{II/III}$, $E_{1/2}$ = 0.830 V, $i_{p,a}/i_{p,c}$ = 0.85.

Ni(L2)(OTf)$_2$ (2). **L2** (0.100 g, 0.245 mmol) was suspended in 10 mL of EtOH. $Ni(OTf)_2$ (0.0873 g, 0.245 mmol) was added, and the mixture was refluxed for 72 h as the solution color slowly turned orange. The solvent was removed, and the residue was redissolved in EtOAc and recrystallized by the addition of hexanes to give yellow block crystals. Yield: 0.110 g, 58.6%. ESI-MS (EtOH): 615.2 $[Ni(\mathbf{L2})(OTf)]^+$; 465.3 $[Ni(\mathbf{L2})-H^+]^+$. Anal. found (calcd) for: C, 43.29 (43.94); H, 5.32 (5.27); N, 7.26 (7.32). Cyclic voltammetry (MeCN under Ar): $Ni^{II/I}$, $E_{1/2}$ = −1.59 V, $i_{p,c}/i_{p,a}$ = 0.95; $Ni^{II/III}$, $E_{1/2}$ = 0.805 V, $i_{p,a}/i_{p,c}$ = 0.96.

Ni(L3)(OTf)$_2$ (3). **L3** (0.500 g, 0.968 mmol) was suspended in 30 mL of EtOH. $Ni(OTf)_2{\cdot}6H_2O$ (0.450 g, 0.968 mmol) was added, and the mixture was refluxed for 24 h as the solution color turned faint orange and a purple precipitate formed. The purple solid was collected by filtration and dried in vacuum. Yield: 0.365 g, 43.0%. ESI-MS (MeCN): 723.1 $[Ni(\mathbf{L3})(OTf)]^+$; 574.2 $[Ni(\mathbf{L3})-H^+]^+$. Anal. found (calcd) for: C, 38.64 (38.51); H, 3.90 (3.92); N, 6.52 (6.41). $Ni^{II/I}$, $E_{p,c}$ = −1.95 V; $Ni^{II/III}$, $E_{1/2}$ = 1.06 V, $i_{p,a}/i_{p,c}$ = 0.90.

Ni(L4)(OTf)$_2$ (4). **L4** (0.100 g, 0.438 mmol) was dissolved in 10 mL of MeOH. $Ni(OTf)_2{\cdot}6H_2O$ (0.203 g, 0.437 mmol) was added, and the mixture was refluxed for 2 h as the solution color turned orange. The solvent was reduced to 1−2 mL, and the product was recrystallized by the addition of Et_2O to give orange block crystals. Yield: 0.105 g, 39.1%. ESI-MS (MeOH): 435.1 $[Ni(\mathbf{L4})(OTf)]^+$; 285.2 $[Ni(\mathbf{L4})-H^+]^+$. Anal. found (calcd) for: C, 29.13 (28.73); H, 4.98 (4.82); N, 9.62 (9.57). $Ni^{II/I}$, $E_{1/2}$ = −1.71 V, $i_{p,c}/i_{p,a}$ = 0.93; $Ni^{II/III}$, $E_{1/2}$ = 0.68 V, $i_{p,a}/i_{p,c}$ = 0.97.

X-ray Data Collection, Processing, and Structure Analysis and Refinement for Crystal Structures. X-ray diffraction data were collected with a Nonius Kappa CCD that used Mo Kα (λ = 0.71073 Å) radiation (**1** and **2**) or a Rigaku RAPID-II image plate diffractometer that used Cu Kα (λ = 1.54184 Å) radiation (**3**). Structures were solved with the aid of the structure solution program DIRDIF2008[60] and refined with SHELX-TLC.[61]

■ ASSOCIATED CONTENT

Supporting Information

The Supporting Information is available free of charge on the ACS Publications website at DOI: 10.1021/acsomega.7b00714.

CV of **1**−**4** in neat MeCN, including anodic peaks; GC calibration curves; and crystal data tables (PDF)

X-ray crystallographic data for the structural determination (CIF)

■ AUTHOR INFORMATION

Corresponding Author

*E-mail: tren@purdue.edu (T.R.).

ORCID

Dennis G. Peters: 0000-0002-3716-8355

Notes

The authors declare no competing financial interest.

CCDC 1559535−1559537 contain the supporting crystallographic data for this paper. These data can be obtained free of charge via www.ccdc.cam.ac.uk/data_request/cif or by emailing data_request@ccdc.cam.ac.uk or by contacting The Cambridge Crystallographic Data Centre, 12, Union Road, Cambridge CB2 1EZ, U.K. Fax: +44 1223 336033.

DOI: 10.1021/acsomega.7b00714
ACS Omega 2017, 2, 3966−3976

■ ACKNOWLEDGMENTS

This work was supported in part by the National Science Foundation (CHE 1609151), Purdue University and the Indiana University.

■ REFERENCES

(1) Fisher, B. J.; Eisenberg, R. Electrocatalytic Reduction of Carbon Dioxide by Using Macrocycles of Nickel and Cobalt. *J. Am. Chem. Soc.* **1980**, *102*, 7361−7363.
(2) Meshitsuka, S.; Ichikawa, M.; Tamaru, K. Electrocatalysis by Metal Phthalocyanines in the Reduction of Carbon Dioxide. *J. Chem. Soc., Chem. Commun.* **1974**, 158−159.
(3) Morris, A. J.; Meyer, G. J.; Fujita, E. Molecular Approaches to the Photocatalytic Reduction of Carbon Dioxide for Solar Fuels. *Acc. Chem. Res.* **2009**, *42*, 1983−1994.
(4) Appel, A. M.; Bercaw, J. E.; Bocarsly, A. B.; Dobbek, H.; DuBois, D. L.; Dupuis, M.; Ferry, J. G.; Fujita, E.; Hille, R.; Kenis, P. J. A.; Kerfeld, C. A.; Morris, R. H.; Peden, C. H. F.; Portis, A. R.; Ragsdale, S. W.; Rauchfuss, T. B.; Reek, J. N. H.; Seefeldt, L. C.; Thauer, R. K.; Waldrop, G. L. Frontiers, Opportunities, and Challenges in Biochemical and Chemical Catalysis of CO_2 Fixation. *Chem. Rev.* **2013**, *113*, 6621−6658.
(5) Benson, E. E.; Kubiak, C. P.; Sathrum, A. J.; Smieja, J. M. Electrocatalytic and Homogeneous Approaches to Conversion of CO_2 to Liquid Fuels. *Chem. Soc. Rev.* **2009**, *38*, 89−99.
(6) Takeda, H.; Cometto, C.; Ishitani, O.; Robert, M. Electrons, Photons, Protons and Earth-Abundant Metal Complexes for Molecular Catalysis of CO2 Reduction. *ACS Catal.* **2017**, *7*, 70−88.
(7) Hawecker, J.; Lehn, J.-M.; Ziessel, R. Electrocatalytic Reduction of Carbon Dioxide Mediated by $Re(Bipy)(CO)_3Cl$(Bipy=2,2′-Bipyridine). *J. Chem. Soc., Chem. Commun.* **1984**, 328−330.
(8) Benson, E. E.; Grice, K. A.; Smieja, J. M.; Kubiak, C. P. Structural and Spectroscopic Studies of Reduced $[Re(bpy\text{-}R)(CO)_3]^{-1}$ Species Relevant to CO_2 Reduction. *Polyhedron* **2013**, *58*, 229−234.
(9) Benson, E. E.; Kubiak, C. P. Structural Investigations into the Deactivation Pathway of the CO_2 Reduction Electrocatalyst $Re(bpy)(CO)_3Cl$. *Chem. Commun.* **2012**, *48*, 7374−7376.
(10) Ishida, H.; Tanaka, H.; Tanaka, K.; Tanaka, T. Selective Formation of $HCOO^-$ in the Electrochemical CO_2 Reduction Catalyzed by $Ru(Bpy)_2(CO)_2^{2+}$ (Bpy = 2,2′-Bipyridine). *J. Chem. Soc., Chem. Commun.* **1987**, 131−132.
(11) Ishida, H.; Tanaka, K.; Tanaka, T. Electrochemical CO2 Reduction Catalyzed by $Ru(Bpy)_2(CC)_2^{2+}$ and $Ru(Bpy)_2(CO)Cl^+$. Effect of Ph on the Formation of CO and $HCOO^-$. *Organometallics* **1987**, *6*, 181−186.
(12) Bolinger, C. M.; Sullivan, B. P.; Conrad, D.; Gilbert, J. A.; Story, N.; Meyer, T. J. Electrocatalytic Reduction of CO2 Based on Polypyridyl Complexes of Rhodium and Ruthenium. *J. Chem. Soc., Chem. Commun.* **1985**, 796−797.
(13) Pugh, J. R.; Bruce, M. R. M.; Sullivan, B. P.; Meyer, T. J. Formation of a Metal-Hydride Bond and the Insertion of Carbon Dioxide. Key Steps in the Electrocatalytic Reduction of Carbon Dioxide to Formate Anion. *Inorg. Chem.* **1991**, *30*, 86−91.
(14) Chen, Z.; Chen, C.; Weinberg, D.; Kang, P.; Concepcion, J. J.; Harrison, D. P.; Brookhart, M. S.; Meyer, T. J. Electrocatalytic reduction of CO2 to CO by polypyridyl ruthenium complexes. *Chem. Commun.* **2011**, *47*, 12607−12609.
(15) Sato, S.; Morikawa, T.; Kajino, T.; Ishitani, O. A Highly Efficient Mononuclear Iridium Complex Photocatalyst for CO2 Reduction under Visible Light. *Angew. Chem., Int. Ed.* **2013**, *52*, 988−992.
(16) Garg, K.; Matsubara, Y.; Ertem, M. Z.; Lewandowska-Andralojc, A.; Sato, S.; Szalda, D. J.; Muckerman, J. T.; Fujita, E. Striking Differences in Properties of Geometric Isomers of $[Ir(tpy)\text{-}(ppy)H]^+$: Experimental and Computational Studies of their Hydricities, Interaction with CO2, and Photochemistry. *Angew. Chem., Int. Ed.* **2015**, *54*, 14128−14132.
(17) Dubois, D. L. Development of Transition Metal Phosphine Complexes as Electrocatalysts for CO_2 and CO reduction. *Comments Inorg. Chem.* **1997**, *19*, 307−325.
(18) DuBois, D. L.; Miedaner, A.; Haltiwanger, R. C. Electrochemical Reduction of carbon dioxide Catalyzed by $[Pd(Triphosphine)\text{-}(Solvent)]$ $(BF_4)_2$ Complexes: Synthetic and Mechanistic Studies. *J. Am. Chem. Soc.* **1991**, *113*, 8753−8764.
(19) Costentin, C.; Drouet, S.; Robert, M.; Savéant, J.-M. A Local Proton Source Enhances CO2 Electroreduction to CO by a Molecular Fe Catalyst. *Science* **2012**, *338*, 90−94.
(20) Costentin, C.; Robert, M.; Savéant, J.-M. Catalysis of the electrochemical reduction of carbon dioxide. *Chem. Soc. Rev.* **2013**, *42*, 2423−2436.
(21) Costentin, C.; Robert, M.; Savéant, J.-M.; Tatin, A. Efficient and selective molecular catalyst for the CO2-to-CO electrochemical conversion in water. *Proc. Natl. Acad. Sci. U.S.A.* **2015**, *112*, 6882−6886.
(22) Weng, Z.; Jiang, J.; Wu, Y.; Wu, Z.; Guo, X.; Materna, K. L.; Liu, W.; Batista, V. S.; Brudvig, G. W.; Wang, H. Electrochemical CO2 Reduction to Hydrocarbons on a Heterogeneous Molecular Cu Catalyst in Aqueous Solution. *J. Am. Chem. Soc.* **2016**, *138*, 8076−8079.
(23) Rail, M. D.; Berben, L. A. Directing the Reactivity of $[HFe_4N(CO)12]^-$ toward H^+ or CO2 Reduction by Understanding the Electrocatalytic Mechanism. *J. Am. Chem. Soc.* **2011**, *133*, 18577−18579.
(24) Taheri, A.; Berben, L. A. Tailoring Electrocatalysts for Selective CO_2 or H^+ Reduction: Iron Carbonyl Clusters as a Case Study. *Inorg. Chem.* **2016**, *55*, 378−385.
(25) Loewen, N. D.; Thompson, E. J.; Kagan, M.; Banales, C. L.; Myers, T. W.; Fettinger, J. C.; Berben, L. A. A Pendant Proton Shuttle on $[Fe_4N(CO)_{12}]^-$ Alters Product Selectivity in Formate vs. H2 Production via the Hydride $[H\text{-}Fe4N(CO)_{12}]^-$. *Chem. Sci.* **2016**, *7*, 2728−2735.
(26) Chakraborty, S.; Zhang, J.; Krause, J. A.; Guan, H. An Efficient Nickel Catalyst for the Reduction of Carbon Dioxide with a Borane. *J. Am. Chem. Soc.* **2010**, *132*, 8872−8873.
(27) Chakraborty, S.; Bhattacharya, P.; Dai, H.; Guan, H. Nickel and Iron Pincer Complexes as Catalysts for the Reduction of Carbonyl Compounds. *Acc. Chem. Res.* **2015**, *48*, 1995−2003.
(28) Dickie, D. A.; Coker, E. N.; Kemp, R. A. Formation of a Reversible, Intramolecular Main-Group Metal−CO2 Adduct. *Inorg. Chem.* **2011**, *50*, 11288−11290.
(29) Dickie, D. A.; Kemp, R. A. Structures and CO2 Reactivity of Zinc Complexes of Bis(diisopropyl-) and Bis(diphenylphosphino)-amines. *Organometallics* **2014**, *33*, 6511−6518.
(30) Barry, B. M.; Dickie, D. A.; Murphy, L. J.; Clyburne, J. A. C.; Kemp, R. A. NH/PH Isomerization and a Lewis Pair for Carbon Dioxide Capture. *Inorg. Chem.* **2013**, *52*, 8312−8314.
(31) Donovan, E. S.; Barry, B. M.; Larsen, C. A.; Wirtz, M. N.; Geiger, W. E.; Kemp, R. A. Facilitated carbon dioxide reduction using a Zn(II) complex. *Chem. Commun.* **2016**, *52*, 1685−1688.
(32) Jin, T.; Liu, C.; Li, G. Photocatalytic CO2 reduction using a molecular cobalt complex deposited on TiO2 nanoparticles. *Chem. Commun.* **2014**, *50*, 6221−6224.
(33) Lin, S.; Diercks, C. S.; Zhang, Y.-B.; Kornienko, N.; Nichols, E. M.; Zhao, Y.; Paris, A. R.; Kim, D.; Yang, P.; Yaghi, O. M.; Chang, C. J. Covalent Organic Frameworks Comprising Cobalt Porphyrins for Catalytic CO_2 Reduction in Water. *Science* **2015**, *349*, 1208−1213.
(34) Balazs, G. B.; Anson, F. C. Effects of CO on the Electrocatalytic Activity of $Ni(cyclam)^{2+}$ toward the Reduction of CO_2. *J. Electroanal. Chem.* **1993**, *361*, 149−157.
(35) Schneider, J.; Jia, H.; Kobiro, K.; Cabelli, D. E.; Muckerman, J. T.; Fujita, E. Nickel(II) Macrocycles: Highly Efficient Electrocatalysts for the Selective Reduction of CO_2 to CO. *Energy Environ. Sci.* **2012**, *5*, 9502−9510.
(36) Fujihira, M.; Hirata, Y.; Suga, K. Electrocatalytic Reduction of CO_2 by Nickel(II) cyclam. *J. Electroanal. Chem.* **1990**, *292*, 199−215.

DOI: 10.1021/acsomega.7b00714
ACS Omega 2017, 2, 3966−3976

(37) Schneider, J.; Jia, H.; Muckerman, J. T.; Fujita, E. Thermodynamics and Kinetics of CO_2, CO, and H^+ Binding to the Metal Centre of CO_2 Reduction Catalysts. *Chem. Soc. Rev.* **2012**, *41*, 2036−2051.
(38) Froehlich, J. D.; Kubiak, C. P. Homogeneous CO_2 Reduction by Ni(cyclam) at a Glassy Carbon Electrode. *Inorg. Chem.* **2012**, *51*, 3932−3934.
(39) Neri, G.; Walsh, J. J.; Wilson, C.; Reynal, A.; Lim, J. Y. C.; Li, X.; White, A. J. P.; Long, N. J.; Durrant, J. R.; Cowan, A. J. A Functionalised Nickel Cyclam Catalyst for CO2 Reduction: Electrocatalysis, Semiconductor Surface Immobilisation and Light-driven Electron Transfer. *Phys. Chem. Chem. Phys.* **2015**, *17*, 1562−1566.
(40) Savéant, J.-M. Molecular Catalysis of Electrochemical Reactions. Mechanistic Aspects. *Chem. Rev.* **2008**, *108*, 2348−2378.
(41) Bujno, K.; Bilewicz, R.; Siegfried, L.; Kaden, T. A. Effects of Ligand Structure on the Adsorption of Nickel Tetraazamacrocyclic Complexes and Electrocatalytic CO_2 Reduction. *J. Electroanal. Chem.* **1998**, *445*, 47−53.
(42) Curtis, N. F. Compounds of Nickel(II) with rac- and meso-5,12-dimethyl-7,14-diphenyl-1,4,8,11-tetraazacyclotetradeca-4,11-diene. *Inorg. Chim. Acta* **2001**, *317*, 27−32.
(43) Hideg, K.; Lloyd, D. Reaction Products from $\alpha\beta$-Unsaturated Ketones and Aliphatic Diamines or Dithiols. *J. Chem. Soc. C* **1971**, 3441−3445.
(44) Curtis, N. F. The Advent of Macrocyclic Chemistry. *Supramol. Chem.* **2012**, *24*, 439−447.
(45) Cook, D. F.; Curtis, N. F.; Rickard, C. E. F.; Waters, J. M.; Weatherburn, D. C. Compounds of Nickel(II) with 5RS,7RS,12SR,14SR-5,12-dimethyl-7,14-diphenyl-1,4,8,11-tetraazacyclotetradecane, mmL2; the Structures of δ-[Ni(mmL2)](ClO4)2, trans-β-[Ni(mmL2)(NO2-N)2] and cis-α-[Ni(mmL2)(acac)]ClO4. *Inorg. Chim. Acta* **2003**, *355*, 1−14.
(46) Kolinski, R. A.; Korybutd, B. Isomeric 5,12-Dimethyl-1,4,8,11-Tetraazacyclotetradecanes and Their Nickel(II) Complexes. *Bull. Acad. Pol. Sci.* **1969**, *17*, 13−18.
(47) Fujita, E.; Haff, J.; Sanzenbacher, R.; Elias, H. High Electrocatalytic Activity of RRSS-[NiIIHTIM](ClO4)2 and [NiIIDMC](ClO4)2 for Carbon Dioxide Reduction (HTIM = 2,3,9,10-Tetramethyl-1,4,8,11-tetraazacyclotetradecane, DMC = C-meso-5,12-Dimethyl-1,4,8,11-tetraazacyclotetradecane). *Inorg. Chem.* **1994**, *33*, 4627−4628.
(48) Anichini, A.; Fabbrizzi, L.; Paoletti, P.; Clay, R. M. Does a Macrocyclic Effect Exist in the Blue-to-Yellow Conversion of Nickel(II) Complexes with Tetra-aza Ligands? *Inorg. Chim. Acta* **1977**, *24*, L21−L23.
(49) Martin, L. Y.; Sperati, C. R.; Busch, D. H. The Spectrochemical Properties of Tetragonal Complexes of High Spin Nickel(II) Containing Macrocyclic Ligands. *J. Am. Chem. Soc.* **1977**, *99*, 2968−2981.
(50) Billo, E. J.; Connolly, P. J.; Sardella, D. J.; Jasinski, J. P.; Butcher, R. J. Conformational Characterization of Square Planar Nickel(II) Tetraaza Macrocyclic Complexes by Proton NMR. Crystal Structure of [Ni(13aneN$_4$)]ZnCl$_4$. *Inorg. Chim. Acta* **1995**, *230*, 19−28.
(51) Boiocchi, M.; Fabbrizzi, L.; Foti, F.; Vázquez, M. Further Insights on the High−low Spin Interconversion in Nickel(II) Tetramine Complexes. Solvent and Temperature Effects. *Dalton Trans.* **2004**, 2616−2620.
(52) Hunter, T. M.; McNae, I. W.; Simpson, D. P.; Smith, A. M.; Moggach, S.; White, F.; Walkinshaw, M. D.; Parsons, S.; Sadler, P. J. Configurations of Nickel-Cyclam Antiviral Complexes and Protein Recognition. *Chem.—Eur. J.* **2006**, *13*, 40−50.
(53) Bieńko, A.; Suracka, K.; Mroziński, J.; Kruszyński, R.; Bieńko, D. C. Synthesis, Crystal Structure and Magnetic Properties of New Molecular, Macrocyclic Building Blocks of Ni(II) and Cu(II). *J. Mol. Struct.* **2012**, *1019*, 135−142.
(54) Vanalabhpatana, P.; Peters, D. G. Catalytic Reduction of 1,6-Dihalohexanes by Nickel(I) Salen Electrogenerated at Glassy Carbon Cathodes in Dimethylformamide. *J. Electrochem. Soc.* **2005**, *152*, E222−E229.
(55) Froehlich, J. D.; Kubiak, C. P. The Homogeneous Reduction of CO_2 by [Ni(cyclam)]$^+$: Increased Catalytic Rates with the Addition of a CO Scavenger. *J. Am. Chem. Soc.* **2015**, *137*, 3565−3573.
(56) Wilson, A. D.; Newell, R. H.; McNevin, M. J.; Muckerman, J. T.; DuBois, M. R.; DuBois, D. L. Hydrogen oxidation and production using nickel-based molecular catalysts with positioned proton relays. *J. Am. Chem. Soc.* **2006**, *128*, 358−366.
(57) Taheri, A.; Thompson, E. J.; Fettinger, J. C.; Berben, L. A. An Iron Electrocatalyst for Selective Reduction of CO2 to Formate in Water: Including Thermochemical Insights. *ACS Catal.* **2015**, *5*, 7140−7151.
(58) Bard, A. J.; Faulkner, L. R. *Electrochemical Methods: Fundamentals and Applications*, 2nd ed.; John Wiley and Sons: New York, 2001.
(59) Kerr, W. J.; Mudd, R. J.; Paterson, L. C.; Brown, J. A. Iridium(I)-Catalyzed Regioselective C−H Activation and Hydrogen-Isotope Exchange of Non-aromatic Unsaturated Functionality. *Chem.—Eur. J.* **2014**, *20*, 14604−14607.
(60) Beurskens, P. T.; Beurskens, G.; deGelder, R.; Garcia-Granda, S.; Gould, R. O.; Smits, J. M. M. *The DIRDIF2008 Program System*; Crystallography Laboratory, University of Nijmegen, The Netherlands, 2008.
(61) Sheldrick, G. M. A Short History of SHELX. *Acta Crystallogr., Sect. A: Found. Crystallogr.* **2008**, *64*, 112−122.

DOI: 10.1021/acsomega.7b00714
ACS Omega 2017, 2, 3966−3976